Laser-assisted photoemission from surfaces

G. Saathoff,[1,*] L. Miaja-Avila,[1] M. Aeschlimann,[2] M. M. Murnane,[1] and H. C. Kapteyn[1]

[1]*Department of Physics and JILA, University of Colorado, Boulder, Colorado 80309-0440, USA*
[2]*Department of Physics, University of Kaiserslautern, Kaiserslautern D-67663, Germany*
(Received 23 November 2007; published 29 February 2008)

We investigate the laser-assisted photoelectric effect from a solid surface. By illuminating a Pt(111) sample simultaneously with ultrashort 1.6 and 42 eV pulses, we observe sidebands in the extreme ultraviolet photoemission spectrum, and accurately extract their amplitudes over a wide range of laser intensities. Our results agree with a simple model, in which soft x-ray photoemission is accompanied by the interaction of the photoemitted electron with the laser field. This strong effect can definitively be distinguished from other laser surface interaction phenomena, such as hot electron excitation, above-threshold photoemission, and space-charge acceleration. Thus, laser-assisted photoemission from surfaces promises to extend pulse duration measurements to higher photon energies, as well as opening up measurements of femtosecond-to-attosecond electron dynamics in solid and surface-adsorbate systems.

I. INTRODUCTION

The development of high intensity ultrashort laser pulses has led to new fields of investigation in strong field physics and nonlinear optics at the extremes of pulse duration, photon energy, and nonlinear response. A number of novel effects have been revealed, including the generation of laser-like beams of xuv light by high-harmonic radiation [1–3]. These beams exhibit low divergence and consist of pulses of very short pulse duration—in the femtosecond-to-attosecond regime—making them a very attractive light source for investigating dynamic processes in atoms, molecules, plasmas, materials, and surfaces. To date, high harmonic beams have been used extensively in ir-xuv geometries, where a visible pump pulse excites dynamics and a time-delayed xuv probe monitors changes in the sample. This approach has been successfully used to study electron relaxation in materials [4–7], surface-adsorbate dynamics [8], photoacoustic dynamics [9], and molecular dissociation [10]. More recently, high harmonics have been used as a pump beam to study x-ray-induced molecular dynamics [11]. Although photon energies >1 keV can be generated using high-harmonic emission, the photon flux is too low above 100 eV to be employed routinely in experiments. In this range of incident photon energies, the high-harmonic light can photoemit valence electrons to high ejected electron energies, well above the ionization threshold of the irradiated gas or solid sample. These electrons are essentially free in the continuum, and the photoelectron energy spectrum then reflects the energy spectrum in the sample with relatively minor need for further interpretation.

Time-resolved experiments using ultrafast high harmonic light have also been greatly expanded by the use of laser-assisted strong-field dynamic processes. When an electron is photoejected in the presence of an intense laser field of larger than about 10^{11} W/cm^2, the electron is accelerated by the laser field. If the interaction occurs continuously over several optical cycles, the electrons undergo oscillations. This leads to ponderomotive energy shifts, and, in the presence of atomic nuclei or solids that can absorb momentum, the generation of sidebands in the photoelectron spectrum corresponding to the absorption and stimulated emission of photons from the laser field.

This laser-assisted photoeffect can be considered to result from "dressing" of the free-electron wave function; i.e., the electron evolves in a state where the free electron is driven by the ir laser field. These dressed states are known as Volkov waves. Laser-assisted electron dynamics were first observed in electron-atom scattering in the presence of a strong CO_2 laser field [12]. Later, this process was applied to time-resolved measurements of laser-assisted Auger decay (LAAD) [13] using ultrashort-pulse soft x-ray plasma sources [14]. Laser-assisted photoemission (LAPE) was first observed by Glover *et al.* [15], using high harmonic sources. In these experiments, atoms are simultaneously irradiated by xuv and intense infrared (ir) light. The presence of the ir laser modifies the xuv photoelectron spectrum. In both cases, LAAD and LAPE, the observation of laser-assisted dynamics of the emitted photoelectrons or Auger electrons indicates the time of their emission. By varying the time delay between the xuv and ir pulses, the LAPE signal provides an exact timing synchronization between the pulses, as well as providing a cross correlation between the laser and xuv fields. More recently, LAPE and LAAD have been combined to measure ultrafast core level dynamics in Krypton atoms [16]. In this experiment LAPE provides time zero, while LAAD yields the emission time behavior of the delayed Auger electrons. In this way, the lifetime of an *M*-shell vacancy in Krypton could be measured directly in the time domain. It has also been shown that with xuv pulse durations in the suboptical cycle domain, LAPE becomes sensitive to the ir electric field rather than the intensity envelope, giving rise to subfemtosecond resolution in time-resolved experiments [17–21]. Recently, LAPE has been successfully demonstrated with femtosecond xuv pulses from the free-electron laser FLASH at DESY in Hamburg [22].

*Present address: Max-Planck-Institut für Quantenoptik, Garching, Germany. Guido.Saathoff@mpq.mpg.de. FAX: (303) 492-5235.

However, with the exception of two very recent experiments [23,24], laser-assisted photoemission and laser-assisted Auger decay have been observed only in gas-phase atomic systems. This limits the current applicability of the physics of laser-assisted dynamics to the study of isolated atoms or molecules. Furthermore, this limitation also represents a practical limit to the use of LAPE for xuv pulse characterization, since both atomic photoionization cross sections and the obtainable photon flux from high-harmonic sources decrease rapidly with increasing photon energy. The result has been that, due to the low target densities in the gas phase, current xuv pulse duration measurements are limited to photon energies below 100 eV. Other approaches for characterizing ultrashort xuv pulses, such as the autocorrelation using two-photon absorption [25,26], are even more experimentally challenging at very high photon energies, and to date have been demonstrated only at photon energies <50 eV.

In a previous Letter, we reported the first experiments to show that the physics of the laser-assisted photoelectric effect can be extended to solid-state systems [23]. This represents the laser-assisted version of the original manifestation of the photoelectric effect, where photons of energy $\hbar\omega$ strike a solid surface with work function W_f and result in ejection of electrons with energy up to $\hbar\omega - W_f$. The goal of this current paper is to show that LAPE can be distinguished from other processes and moreover, that it is possible to perform experiments over a wide range of intensities where LAPE is the dominant process in strong-field interaction with solids.

In our work, a clean Pt(111) single crystal was used as the solid surface, since it exhibits a large density of d states at the Fermi edge, with a characteristic peaklike structure in the xuv photoelectron spectrum. In the presence of an intense laser field, sidebands appear in the Pt(111) photoemission spectrum. We show that the modification of the photoelectron spectrum by LAPE can be distinguished from simple heating of the electrons by the ir beam by varying the laser polarization, by measuring the mean energy of the photoejected electrons and verifying that it does not change, and by successfully fitting the photoelectron spectrum to theory. We also demonstrate that the surface LAPE can be used to measure the pulse duration of our xuv beam.

This result is significant for three reasons. First, the surface LAPE has the potential to study ultrafast, femtosecond-to-attosecond time-scale electron dynamics in solids and in surface-adsorbate systems—where complex, correlated, electron relaxation processes are expected. This is in contrast with measurements to date in atomic systems, where dynamics are generally only homogeneously broadened and where time-domain studies have duplicated information that can be obtained from spectroscopic studies. Second, surface LAPE will make it possible to characterize lower-flux and higher-energy xuv pulses, because of the orders-of-magnitude higher density of target atoms on a surface compared with a gas—which is typically limited to ≪1 mbar pressure to allow for sufficient electron mean free path in the experiment. Finally, this result represents new physics—the extension of atomic dressed states to surface dressed states is not obvious, because of complex spatially dependent laser electric fields present at the surface.

In the next two sections we discuss laser-assisted photoemission from atoms and solids, respectively. We then describe our experimental setup, and several effects such as above-threshold photoemission, the observed sideband structure and its intensity, angle, and polarization dependence. We also discuss data on space-charge and hot electron effects, and show that we can operate over a wide parameter range where the laser-assisted photoemission dominates our experimental signal.

II. LASER-ASSISTED DYNAMICS IN ATOMS

We recall here the basic picture of strong-field laser-assisted dynamics, for the limiting case where the electrons interact with the driving ir laser over many optical cycles. The exchange of photons between free electrons and a strong laser field is forbidden because energy and momentum cannot be conserved simultaneously. The situation changes if a heavy particle such as an atom or molecule or solid are available to balance momentum conservation. As a result laser-induced "free-free" transitions can occur, along with electronic processes such as Auger decay, photoemission, and electron-atom scattering, where electrons reside in the continuum spectrum of the particle involved. Especially in the far-from-threshold case, these electrons behave essentially as free electrons, with a wave function approximately described by plane waves with momentum $\boldsymbol{p}$ (in atomic units $\hbar = e = m = a_0 = 1$), $\psi_p(r,t) = (2\pi)^{-3/2} \exp i[\boldsymbol{p}\cdot\boldsymbol{r} - p^2 t/2]$ in the field-free case.

If these electrons are exposed to a strong low-frequency laser field of vector potential $\boldsymbol{A} = \boldsymbol{A}_0 \cos \omega_{ir} t$, the quasifree electrons are ponderomotively shifted and undergo transitions between continuum states by exchanging photons with the laser field (Fig. 1). In the so-called soft-photon limit, where the kinetic energy of the electrons is large compared to the dressing laser photon energy ($E_{kin} \gg \omega_{ir}$), the interaction can be modeled quasiclassically as an oscillatory motion with an amplitude A_0/ω_{ir} of the electron in the laser field. By inserting $\boldsymbol{r} \rightarrow \boldsymbol{r} - (\boldsymbol{A}_0/\omega_{ir})\cos \omega_{ir} t$ into the plane wave and performing a Fourier transform, the electron wave function becomes

$$\Psi = \exp\left[i\left(\boldsymbol{p}\cdot\boldsymbol{r} - \frac{p^2}{2}t \right) \right]\left[\sum_n J_n\left(\frac{\boldsymbol{p}\cdot\boldsymbol{E}_0}{\omega_{ir}^2} \right)\exp(-in\omega_{ir}t) \right],$$

(1)

with $\boldsymbol{E}_0 = \omega_{ir}\boldsymbol{A}_0$. This can be viewed as a frequency-modulated plane electron wave. The presence of a Bessel function is a characteristic feature of laser-assisted dynamics. In the soft photon limit, the interaction depends solely on the momentum of the electron as well as on the intensity and frequency of the dressing laser—but not on properties of the target atom. In this approximation, the target atomic potential only enables momentum conservation but does not further influence the spectrum. Quantum mechanically, the Schrödinger equation of a free electron in a strong field is solved by the Volkov wave functions
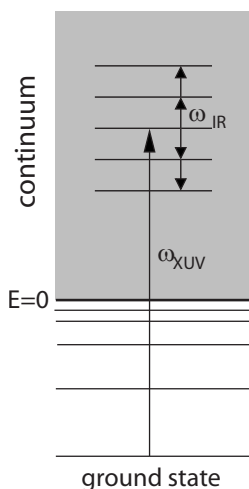
FIG. 1. The principle behind the laser-assisted photoemission process for atoms in the "soft photon" limit. LAPE is described in two steps. First, the ground state electron is photoemitted into an excited state in the continuum by the xuv pulse, neglecting the influence of the ir field. Then the photoemitted electron evolves as a free electron in the ir field, unaffected by the atomic potential. This results in a redistribution of the electrons in the continuum by absorption and stimulated emission of ir photons.

$$\psi_V(\vec{r},t) = \frac{1}{(2\pi)^{3/2}} \exp(i\boldsymbol{p} \cdot \boldsymbol{r}) \sum_{n=-\infty}^{\infty} J_n\left(\frac{\boldsymbol{p} \cdot \boldsymbol{E}_0}{\omega_{ir}^2}, \frac{U_p}{2\omega_{ir}}\right)$$
$$\times \exp[-i(p^2/2 + U_p + n\omega_{ir})t], \qquad (2)$$

which are momentum eigenfunctions. Here $U_p = E_0^2/4\omega_{ir}^2$ is the ponderomotive potential, n is the number of exchanged photons, and $\boldsymbol{p}$ is the electron momentum for the field-free case. Here $J_n(a,b)$ denotes the generalized Bessel functions [27]. For $b=0$, i.e., negligible ponderomotive potential, they reduce to the ordinary Bessel functions $J_n(a,0) = J_n(a)$.

In the photoelectric effect, an electron is photoemitted from a gaseous or solid sample by a high-energy photon ω_X. In the presence of a sufficiently strong low-frequency laser field, the photoelectron is emitted into a Volkov state so that it undergoes the dynamics described by the generalized Bessel function in Eq. (2). The laser field induces a ponderomotive shift, as well as a redistribution of these electrons into sidebands separated by one photon energy ω_{ir} from the original energy in the kinetic energy spectrum. For high electron kinetic energies and low laser frequencies, this process can be described in an approximation similar to the "simpleman's theory" [28]. In this model, LAPE is considered as a two-step process. The first step is the xuv photoemission of an electron unaffected by the ir laser field. This is justified at moderate laser intensities, because the initial ground states are more tightly bound to the nuclei than the continuum electrons, and are thus only slightly affected by the laser field. In the second step, the released electron evolves in the laser field and is unaffected by the target potential. The interaction of the electron with the laser field in the continuum can thus be described using the Volkov wave function as a final state of the xuv photoemission process.

In the field-free case, the S matrix for the xuv photoelectric effect from a ground state $\Phi_0 = \phi_0(\mathbf{r})e^{iE_bt}$ with the binding energy E_b into the final state ψ_p of momentum p is then given by

$$(S-1)_{fi} = -i \int_{-\infty}^{\infty} dt \langle \psi_p | \boldsymbol{A}_X(t) \cdot \boldsymbol{p} | \Phi_0 \rangle, \qquad (3)$$

where $\boldsymbol{A}_X(t)$ is the vector potential of the xuv light in the dipole approximation and thus omitting the spatial dependence e^{ikr}. To calculate the laser-assisted version of this process, the plane wave in the final state is replaced by a Volkov wave ψ_V of the same momentum p as follows:

$$(S-1)_{fi} = -i \int_{-\infty}^{\infty} dt \langle \psi_V | \boldsymbol{A}_X(t) \cdot \boldsymbol{p} | \Phi_0 \rangle. \qquad (4)$$

In this approach, the influence of the ir field $\boldsymbol{A}$ on the initial state, as well as the influence of the sample potential V on the final continuum state, are neglected. The former is justified even for weakly bound systems as long as V is a short-range potential [27], while the latter holds in the soft photon limit. From these two S-matrix elements, the ratio of the laser-assisted and the field-free photoemission cross sections can be derived [29] as follows:

$$A_n = \frac{d\sigma^{(n)}/d\Omega}{d\sigma/d\Omega} = J_n^2\left(\frac{\boldsymbol{p} \cdot \boldsymbol{E}_0}{\omega_{ir}^2}, \frac{U_p}{2\omega_{ir}}\right) \approx J_n^2\left(\frac{\boldsymbol{p} \cdot \boldsymbol{E}_0}{\omega_{ir}^2}\right). \qquad (5)$$

In the approximation of Eq. (5), the ponderomotive potential is neglected. As is the case in the soft photon limit, the target atom properties cancel and the sideband amplitude depends only on the electron and ir light properties. It is therefore expected that, to the extent that the soft photon approximation is justified, target properties are negligible.

III. ASPECTS OF SURFACE LAPE

In principle, the concept of the laser-assisted photoelectric effect should also apply to solid surfaces, and should result in the convolution of sideband shifts onto the entire continuous xuv photoemission spectrum from the solid. However, due to the manifold different excitation paths and energy dissipation channels, the interpretation of energy shifts in the photoemission spectra from solid surfaces is more complicated than in the gas phase. In the following we discuss possible influences of the strong ir light on the photoemission spectra from solids.

A. Momentum conservation and ground state dispersion

A basic difference between photoemission from crystal surfaces, when compared to photoemission from atoms, concerns the exchange of momentum. This is restricted to integer multiples of the reciprocal lattice vector $\hbar\boldsymbol{G}$ in a crystal, due to the periodicity of the lattice. However, the presence of a surface removes the periodicity in one half-space and softens momentum conservation. In the case of xuv photoemission, the electrons have a very short escape depth of the order of 5 Å, according to the universal curve [30,31]. They

thus sense only one or two atomic layers. The surface *can* then act as a continuous source or sink of momentum normal to the surface [32], and the electron can be excited into a surface state, often called the inverse low energy electron diffraction (LEED) state. Along the surface normal, the latter is essentially a plane wave. For an ir laser pulse impinging on a metal surface, the electric field components parallel to the surface nearly vanish because of the boundary conditions. The remaining field, i.e., the component that is able to dress the photoemitted electrons, thus points along the surface normal, where the surface can balance momentum conservation. In this direction, the interaction of the emitted electron with the ir laser can be described by replacing the plane wave part of the LEED final state by a Volkov wave.

However, in xuv photoemission, part of the spectrum arises from direct transitions, e.g., the emission from d bands into s bands in transition metals. This photoemission process conserves the momentum $q_\parallel$ parallel to the surface. As the "dressing" is associated with a momentum change along the surface normal, the direction of emission of the electron is in general changed, except for electrons emitted normal to the surface. For angle-resolved photoemission spectroscopy with infinite resolution, this means that in laser-assisted photoemission, the detected sidebands stem from electrons emitted from different initial states and at slightly different angles compared with the electrons that did not lose or gain photons of energy $\hbar\omega$ from the ir field. Due to the dispersion of the valence bands in solids, the corresponding energies can be shifted leading to a deviation of the sideband energy spacing compared with the ir photon energy. However, in the soft photon limit, the relative momentum change associated with the exchange of a photon between the photoelectron and the ir field is small. At an observation angle of 45°, the absorption or emission of a 1.6 eV photon by a 36 eV electron leads to $\Delta k_\parallel = 0.05$ Å^{-1}, which is about 0.02 of the total Brillouin zone. The corresponding energy shift due to dispersion is at most 50 meV, which is significantly smaller than the ir photon energy (1.59 eV) and even below the energy resolution of our detector. Thus, we neglect these dispersion energy shifts in this work.

B. Resonant interband and intraband transitions

Another difference between atoms and surfaces is the quasifree behavior of electrons in a band, due to the delocalization of the electrons from individual ions. At the Fermi edge of Pt however, the energy spectrum is dominated by d bands, which deviate significantly from the free-electron-like sp bands. Due to the strong localization of the d electrons to the crystal ions, the d bands are narrow and exhibit only low dispersion. They can be described in the tight-binding approximation and resemble bound electrons in atoms [33]. Ground state dressing of the d electrons is therefore neglected in the soft photon limit for the same reasons as in atoms [34]. For the broader sp bands, the tight-binding approximation does not hold. However, although the electrons can move freely, they cannot respond to the ir light in the same way as electrons in the continuum. At low frequencies, the interaction of light with a metal is dominated by intra-band absorption. In this process, which corresponds to the classical ir absorption picture, electrons can absorb any photon energy from the ir field and are promoted into unoccupied levels above the Fermi edge. This mechanism thus only affects a small fraction of the electrons, in a narrow window around the Fermi edge, and does not lead to sideband peaks. Moreover, resonant $k_\parallel$-conserving interband transitions are only possible in certain directions when energy and momentum conservation are fulfilled. Contrary to the case of continuum electrons, only absorption is possible from the ground state, because stimulated emission is forbidden by the Pauli principle as the lower lying states are filled. The presence of such resonant interband transitions should thus be visible by an enhancement of the positive sideband; i.e., conduction-band electrons can absorb photons from the laser field. The dependence of this contribution on the ir-xuv time delay should follow the lifetime of the intermediate states, which is of the order 100 fs for transition metals [35]. Both effects are not observed in our experiment.

C. Nonresonant interband transitions

Due to the high ir intensities applied in LAPE experiments, nonresonant ir interband transitions into virtual levels occur which can serve as intermediate states for multiphoton ionization. Such transitions have been studied theoretically in atoms in different limiting cases. For electrons in excited Rydberg states of atoms, nonresonant absorption and emission of microwave photons into virtual states can lead to dressing analogous to the continuum [36]. As unoccupied real levels above and below the initial Rydberg state are densely spaced, both absorption and emission are equally likely, which leads to symmetric sidebands. For electrons in an atomic ground state, symmetric sidebands can occur when the photon energy of the dressing beam is considerably smaller than the spacing between the atomic levels. In this case, which is usually fulfilled only for light in the far ir or microwave region, the distance of the virtual states after absorption and emission are approximately equally spaced from the closest unoccupied level [37].

In our experiment, the electrons are in the ground state and the photon energy is not resonant with an interband transition. Nonresonant absorption is closer to resonance with an unoccupied real state than stimulated emission, since unoccupied levels are only available above the ground state. Dressing of the ground state is thus expected to preferentially enhance the positive sideband leading to asymmetric amplitudes. In the light-metal interaction volume, however, the electron number reaches the same order of magnitude as the number of photons per pulse applied in our experiment. As a consequence, only a very small fraction of the electrons is excited into the virtual states, leading only to a negligible contribution to the positive sideband in the xuv photoemission spectrum. This is in contrast to gaseous atoms where the atom density is usually much lower than the photon density. In the case of dressing of the final state, only the small number of photoemitted electrons plays a role—so that in the continuum, a significant fraction of the electrons can be dressed.
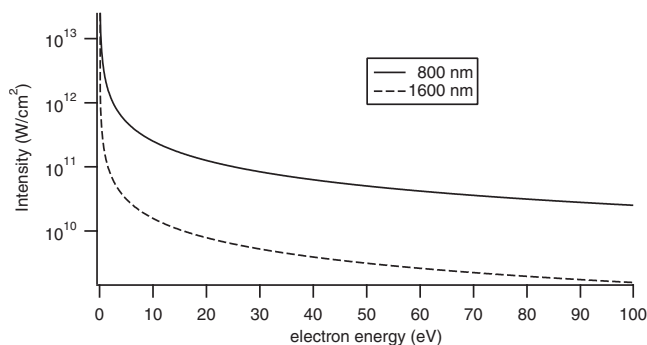
FIG. 2. Calculated ir intensity required to generate first-order sideband heights of $A_1 = 0.1$ for wavelengths of 800 and 1600 nm, respectively, as a function of the kinetic energy of the electrons. For kinetic electron energies of 36 eV and an 800 nm dressing wavelength, laser intensities greater than 10^{11} W/cm^2 are required.

D. Dressed band structure

Theoretical investigations of intense field effects in solids predict the opening of band gaps [38,39] whenever direct multiphoton transitions are possible. These band gaps are closely related to the intensity-dependent Autler-Townes splitting [40] of atomic levels in the presence of a resonant or near-resonant strong laser beam. At a photon energy of 1.6 eV, the laser is not resonant with any direct interband transition [41], so that ground state dressing is expected to play a minor role in our experiment. The strong ir laser thus influences the electrons only after photoemission, leading to the final state dressing picture similar to the experiments done in gaseous atoms.

E. Competing strong-field effects

For applications of LAPE in xuv pulse duration measurements, the sideband amplitude range, after Eq. (5) $A_n = J_n^2(x)$ for small values of the argument x is of special interest. In système international d' unités (SI) units x can be written as

$$x = \sqrt{\frac{16\pi\alpha}{m_e\hbar}\frac{IE_{kin}}{\omega_{ir}^4}}.\qquad(6)$$

For small x, A_1 can be approximated by $A_1 \approx x^2/4$ leading to

$$A_1 \propto \frac{IE_{kin}}{\omega_{ir}^4}.\qquad(7)$$

In this regime, the sideband height depends linearly on the ir laser intensity, which makes it a suitable observable for xuv-ir cross-correlation measurements as well as for time-resolved spectroscopy. Additionally, A_1 depends on the kinetic energy E_{kin} of the dressed electron and on the ir photon energy ω_{ir}. Figure 2 shows the intensity required to generate first-order sideband amplitudes of $A_1 = 0.1$ versus the photoelectrons' kinetic energies E_{kin} for 800 nm light. For kinetic energies below 100 eV, an intensity of at least 10^{11} mW/cm^2 is necessary. For slower electrons, the required intensity increases dramatically. This intensity range is only one to two

orders of magnitude below the damage threshold of metal surfaces. Also, the excitation of nonthermal hot electrons leads to changes in the spectra similar to those caused by the photoelectric effect. Finally, the illumination of metal surfaces at such high intensities leads to significantly stronger electron emission and higher kinetic energies than from gaseous atoms, due to field enhancement and space-charge-induced Coulomb explosion.

In past work, it was shown that above-threshold photoemission (ATP) can be significant from surfaces at much lower laser intensities than in atoms due to field enhancement effects [42]. Above-threshold photoemission is the photoemission of electrons from a surface by absorption of more photons than is required to overcome the work function. This effect can be understood, similar to LAPE, by the rate-limiting multiphoton ionization of the sample by absorption of the minimum number of photons needed, and followed by redistribution of these electrons in the continuum by absorption of additional photons [28]. For ultrashort Ti:sapphire laser pulses at 780 nm, intensities of the order of 10^{14} W/cm^2 are needed to cause a substantial emission of electrons by multiphoton ionization of gaseous atoms; i.e., above-threshold ionization. However, it has been known for a long time that surface plasmons can lead to substantial field enhancement (up to a factor of 10^3) corresponding to intensity enhancements of 10^6 on a metal surface. This effect results in phenomena such as surface-enhanced Raman scattering. Although forbidden by energy and momentum conservation on perfectly flat surfaces, these surface plasmons can be excited on rough surfaces. Due to the corresponding field enhancement, ATP can happen at intensities as low as 10^8 W/cm^2 [42]. These enhancements not only lead to higher kinetic energies of the ATP electrons than the corresponding above threshold ionization (ATI) from atoms, but furthermore the number of electrons is considerably larger. Additionally, the first step in ATP—multiphoton ionization—is stronger than in atoms, because of the low ionization potential (work function) of solids. Finally, the sample particle density is higher than in typical experiments on atoms. As a consequence, many electrons can be emitted from a very small volume of the solid sample by a single intense laser pulse. This leads to a Coulomb explosion as the electrons repel each other [43,6]. This way some of the electrons are accelerated and can gain a significant amount of extra kinetic energy, while others are decelerated and may not escape the surface. Surface preparation thus plays a major role in the ability to successfully observe LAPE.

The purpose of this work is to extract from ir-xuv photoemission data unambiguous signatures of all the processes that occur when a surface is illuminated simultaneously with an xuv and intense ir fields, i.e., ATP, heating of the valence electron distribution, and LAPE. Comparing the relative magnitudes of these effects allows us to develop methods to unambiguously single out the continuum free-free transitions corresponding to LAPE. We find that LAPE is the dominant process over a wide range of ir intensities and polarizations typically employed in experiments investigating charge transfer dynamics in surfaces and surface-adsorbate systems. This result shows the feasibility of extending the variety of time-resolved measurements using LAPE that have been ob-
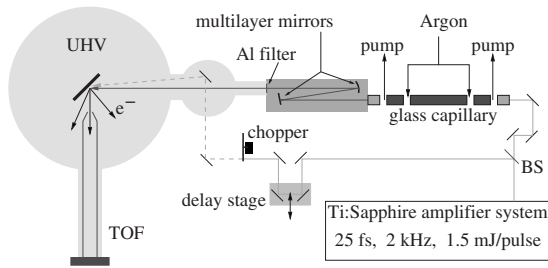
FIG. 3. Experimental setup for observing the laser-assisted photoelectric effect from surfaces. ir pulses from a Ti:sapphire laser amplifier are split into two. One beam is directed onto the surface through a variable optical delay stage and an optical chopper running at half the repetition rate of the laser. The other beam is upconverted into the xuv regime using phase-matched HHG in an Argon-filled glass capillary. Two multilayer mirrors select the 27th harmonic at 30 nm/42 eV and focus it onto the Pt(111) sample inside a uhv chamber. The crystal is mounted on a rotation stage and cooled to liquid nitrogen temperature. A TOF detector measures the kinetic energies of the photoelectrons emerging from the sample.

served and employed in atomic and molecular samples, to solid surfaces.

IV. EXPERIMENTAL SETUP

Figure 3 shows the experimental setup. A temperature-controlled Pt(111) sample is mounted on a translation and rotation stage inside an ultrahigh vacuum (uhv) chamber. To avoid quenching of the peaklike d-band structure at the Fermi edge by adsorption of contaminants, the sample is cleaned at regular intervals using three cycles of annealing with oxygen at 920 K and flashing to 1300 K. At the base pressure of 3×10^{-10} mbar, the Pt surface stays clean for several hours. For the measurements, the sample was cooled to 84 K using liquid nitrogen.

A Ti:sapphire multipass amplifier laser system producing 1.5 mJ, 780 nm pulses at a repetition rate of 2 kHz, and with a duration of 25 fs is used to generate the ir and xuv beams [44]. Approximately 30% of the laser energy is used for the ir dressing beam, while the remaining 70% are upconverted by phase-matched high-harmonic generation in an argon-filled hollow waveguide [45]. A pair of Si:Mo multilayer mirrors—one flat and one curved—is used to spectrally select the 27th harmonic (at a wavelength of 30 nm, corresponding to a photon energy of 42 eV) and to focus this xuv beam onto the Pt surface in a beam with a spot size of the order of 100 μm. Additionally, an aluminum filter of 200 nm thickness is used to maintain a pressure differential between the high-order harmonic generation (HHG) cell and the uhv chamber, and to block the copropagating ir light while transmitting the xuv beam. As shown in Fig. 4, the xuv beam, containing about 10^6 photons per pulse after these optical elements, irradiates the sample at a variable angle θ with respect to the surface normal. The kinetic energies of the photoemitted electrons are analyzed at 90° with respect to the incoming xuv beam, using a 600-mm-long time-of-flight
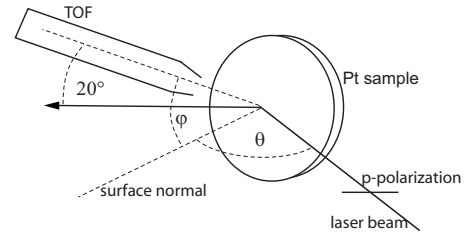

FIG. 4. Geometry for the LAPE measurements: p-polarized ir light impinges on the Pt sample at an angle θ with respect to the surface normal. $\vartheta = 90 - \theta$ is the angle of the polarization vector with respect to the surface normal. The detector is tilted by 20° with respect to the plane of incidence. The corresponding observation angle φ with respect to the surface normal is given by $\cos \varphi = \cos 20° \cos \vartheta$.

detector (TOF). Its angular acceptance is $\pm 2°$, corresponding to a solid angle of 3×10^{-4} steradians. In order to prevent light reflected off the sample hitting the detector, the TOF tube is tilted up with respect to the plane of incidence by an angle of 20°. Consequently the observation angle ϕ with respect to the surface normal is given by $\cos \phi = \cos 20° \cos(90 - \theta)$.

The ir beam is directed onto the surface through a variable optical delay stage and focusing lens, and overlaps with the xuv beam on the sample at a small (1°) angle. Its pulse duration is broadened to $\approx 35-40$ fs by dispersion as it propagates through various optical elements in the delay line. The maximum ir power available is 300 mW, and the beam spot size is varied between 0.4 and 1.2 mm by moving the focusing lens. The ir beam is chopped at 1 kHz, and the TOF detector is gated to record ir-xuv and xuv-only spectra alternately. This allows us to distinguish between emission caused solely by the ir beam (such as above-threshold photoemission) from two-color (ir-xuv) photoemission. Moreover, the availability of both ir-xuv and xuv-only spectra makes it possible to unambiguously observe the laser-induced free-free transitions in the continuum, as will be discussed further below.

The spatial and temporal overlap between the ir and the xuv beams at the sample is obtained using a multistep procedure. A preliminary spatial overlap is obtained by moving the sample holder so that the two beams hit a phosphor screen that is moved in place of the Pt(111) surface. The beams are observed and aligned using a charge-coupled device (CCD) camera that images the phosphor from outside the chamber. The temporal overlap is obtained by moving the sample holder to another position, where the beams pass through a BBO frequency-doubling crystal. The aluminum filter in the xuv beamline is replaced by a thin (0.355 mm) sapphire window to allow the ir light from the high-harmonic xuv beamline into the uhv chamber. A cross correlation between the two ir fields then locates time zero. The position of time zero must be corrected for the sapphire window group delay, which is 934 fs. At this point, the Pt(111) sample is moved into place. Since the position of the phosphor screen along the light direction is not exactly the same as the Pt(111) sample, the spatial overlap must be readjusted. This is done using LAPE itself, by observing the highest-energy

photoelectrons as a measure of spatial and temporal overlap.

A. Above-threshold photoemission

As has been discussed above, the ir laser intensity at 800 nm required to generate sidebands is of the order of 10^{11} W/cm². Since the parallel component of the electric field nearly vanishes at the surface of a good conductor, the laser polarization must be perpendicular to the surface. Figure 5 shows a photoemission spectrum taken for *p*-polarized ir light as the laser intensity is varied around 10^{11} W/cm². No xuv light was incident in this measurement. Since the ponderomotive potential at these intensities is <0.1 eV and is much less than the work function of Pt (5.8 eV), no "channel-closing" occurs, and at least 4 ir photons are required to photoeject electrons from the surface. The lowest intensity curve basically shows multiphoton photoemission by four photons, with a small contribution of above-threshold photoemission by five photons. As the intensity is increased, two effects can be observed. First, above-threshold photoemission becomes stronger. The five-photon edge increases and new channels with six and seven photons appear. However, at higher laser intensities the separations of subsequent edges are measurably larger than the ir photon energy. This is due to the fact that the number of photoelectrons increases dramatically and leads to a Coulomb explosion of the electron cloud due to their mutual repulsion [6]. As a result, faster electrons at the front of the cloud are accelerated, while slower electrons at the back are decelerated. This effect already becomes very strong at the moderate laser intensities applied here. In contrast to experiments on gaseous samples, the higher target densities and lower ionization potentials in solids lead to stronger multiphoton ionization, above-threshold photoemission, and as a consequence, also to stronger space-charge acceleration. To detect LAPE from solids with Ti:sapphire laser pulses at 800 nm, xuv photon energies of at least 30–40 eV are required so that the photoejected electrons corresponding to the Fermi edge have energy significantly higher than the IR-induced ATP electrons. However, even if the xuv photoelectron Fermi edge lies beyond the high-energy ATP electrons, its shape can still be altered by the space charge if too many ir-induced electrons are emitted. It is therefore important to reduce space-charge effects as much as possible.

The measurement shown here was performed on a sample that was cleaned as described above. This is necessary since any surface roughness can lead to strong local enhancements of the ir field at the surface [42] which dramatically increases the number and energy of ir-ejected electrons. Due to the strong susceptibility of these effects to surface roughness, the ir-induced electron spectra differ strongly from day to day, and Fig. 4 can thus only be taken as an example. We observe the creation of hot spots on the Pt(111) surface resulting from ir laser intensities above $\sim 10^{12}$ W/cm² at pulse duration ~ 30 fs. These hot spots result in a huge increase in high-energy electrons resulting from the ir field. Apart from using shorter pulse durations to raise this damage threshold, the use of lower ir photon energy as the dressing field would help to circumvent this problem. Due to the ω_{ir}^{-4} dependence
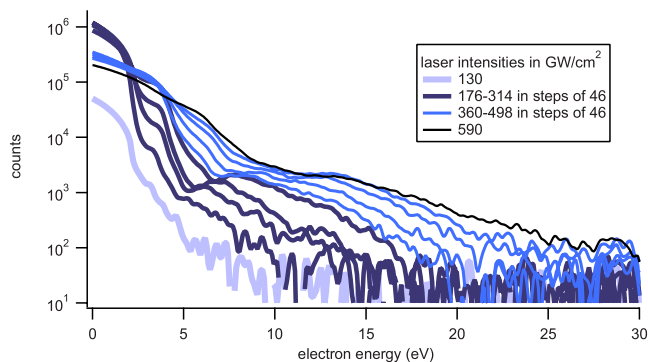

FIG. 5. (Color online) Photoemission spectra taken at different laser intensities ranging from 130 to 590 mW/cm² using ir light only. ATP (above-threshold photoemission) and space-charge acceleration generate electrons with kinetic energies of tens of eV.

of the sideband amplitudes in Eq. (7), increasing the wavelength of the ir by a factor of 2 would reduce the intensity required to generate sidebands by a factor of 16. High-power optical parametric amplifiers [46] would thus facilitate LAPE experiments on metal surfaces. In the present experiment however, ir-induced electrons can be kept sufficiently low by thorough sample preparation and by restricting the ir laser intensity to moderate values.

B. Extraction of the sideband structure

As mentioned before, LAPE has been extensively studied in the gas phase, where the discrete nature of the photoelectron spectrum makes the sidebands easy to distinguish. To extract this peaklike sideband structure from the continuous spectra of solid surfaces, the ir-xuv spectrum must be deconvolved from the xuv-only spectrum using a fitting procedure. Figure 6 shows a series of photoelectron spectra around the Fermi edge, at an ir peak intensity of the order of 10^{11} W/cm² and for relative time delays between the ir and xuv beams ranging from −100 fs to +100 fs. Negative time delays mean that the ir pulse comes after the xuv pulse. The ir beam was polarized in the plane of incidence (*p* polarized). The xuv-only spectrum is only shown for the −100 fs measurement (dashed line). At this time delay, both the xuv-only, as well as the ir-xuv spectra, show the typical *d*-band structure of clean Pt(111). This Pt *d*-band peak near the Fermi edge, although 0.9 eV wide, is nevertheless a very useful characteristic peak around which to observe sidebands. While the spectral shape is unaffected by the presence of the ir field, the ir-xuv spectrum is slightly shifted to higher electron energies as compared to the xuv-only spectrum due to the space-charge-induced Coulomb explosion. We have observed this space-charge-induced shift to be present for time delays between at least −1 ps and +1 ps. This can be explained by the fact that the photoemitted electrons are traveling slowly enough that they do not escape from the range of the space-charge field of the ir-induced electron cloud during the time frame of the experiment. Thus, the xuv photoelectron energies are slightly shifted even when the ir pulse comes considerably after the xuv. This space-charge effect
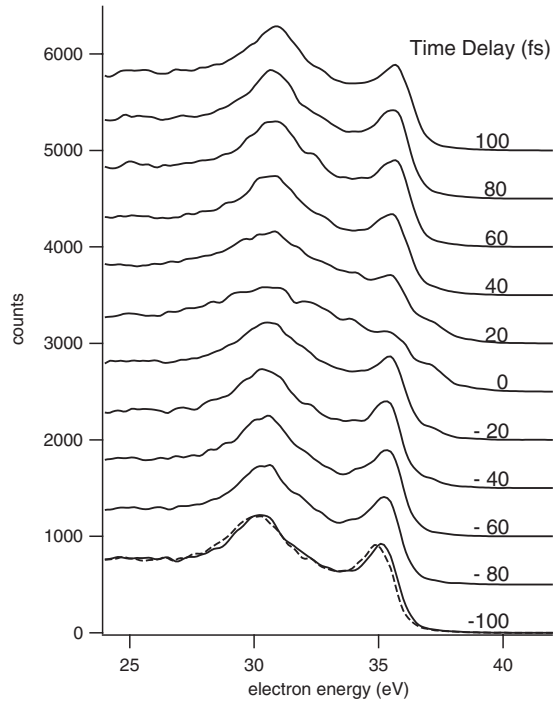
FIG. 6. Observed photoelectron spectra from Pt(111) as a function of time delay between the ir and xuv beams. For −100 fs time delays, the xuv-only spectrum (dashed line) is also shown. A slight shift of the spectrum due to ir-induced space charge can be seen, but this does not change the shape of the spectrum and can thus be corrected for. The strong modification at the Fermi edge of the time zero spectrum is due to laser-assisted photoemission.

increases strongly with the ir intensity. At very high intensities it not only shifts the ir-xuv spectra but also changes its shape (see, e.g., Fig. 16). However, in Fig. 6, the space-charge effect is rather low, indicating an effective ir intensity in the low 10^{11} W/cm^2 range. The space-charge shift is determined from the −100 fs curves and all ir-xuv spectra are corrected for it before subsequent analysis.

In the photoemission spectrum shown in Fig. 6 near that which corresponds to zero time delay between the laser and xuv pulses, we observe a very strong shape change at the Fermi edge. Insight into the origin of this change can be gained by calculating the average kinetic energy of the photoelectrons above 20 eV, both with and without the ir pulse present. (Below 20 eV photoelectron kinetic energies, the ir-xuv spectrum is dominated by low-energy electrons from above-threshold photoemission.) No significant ir-induced increase of the average kinetic energy was found around zero fs. Indeed, the calculated average photoelectron kinetic energies with and without the ir were identical, within 0.1 meV, at all time delays. This indicates an essentially equal redistribution of electrons to lower and to higher kinetic energies in the presence of the ir field that modifies the photoelectron spectra. This result therefore excludes interpretations of a photoelectron spectrum modified by image potential states, ground state dressing, or hot electrons, [47] since in all cases, the average kinetic energy should be increased by the presence of the ir field. We therefore interpret the Fermi edge modification near time zero to be the result of the laser-
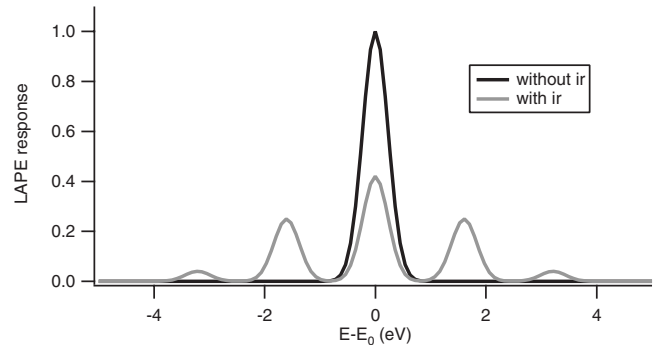

FIG. 7. Calculated LAPE response function using Eq. (8) assuming the generation of two sidebands.

assisted photoelectric effect. Viewed in a perturbative two-step model, the electrons photoemitted by the xuv beam can absorb or emit photons from the ir field, leading to sidebands in the photoelectron spectrum. In an atomic system, the xuv photoelectron spectrum consists of discrete atomic peaks, and the LAPE sidebands are easily distinguished. From a surface, the photoemission spectrum consists of a continuous distribution due to the band structure of the solid. Nevertheless, the high density of states at the Fermi edge for Pt(111) does allow one to discern sideband peaks at ±1.6 eV.

To quantitatively extract the sideband intensities in the case of photoemission from Pt in the presence of an intense ir field, we modeled the absorption and emission of up to two ir photons by a photoelectron of kinetic energy E_0 by

$$f(E - E_0) = \frac{1 - 2A_1 - 2A_2}{\sqrt{2\pi\sigma^2}} e^{(E - E_0)^2/2\sigma^2}$$
$$+ \sum_{\pm} \left(\frac{A_1}{\sqrt{2\pi\sigma^2}} e^{(E - E_0 \pm \hbar\omega)^2/2\sigma^2} \right.$$
$$+ \left. \frac{A_2}{\sqrt{2\pi\sigma^2}} e^{(E - E_0 \pm 2\hbar\omega)^2/2\sigma^2} \right) \qquad (8)$$

(see Fig. 7). Since the kinetic energies of the affected electrons are large compared to the ir photon energy (soft photon limit), we assume that the influence of the ground state on the free-free transitions is negligible. In particular, the above LAPE response function is considered independent of the electron's kinetic energy over the fit range around the Fermi edge. Consequently, the ir-xuv spectrum is expected to be generated by a convolution of the xuv-only spectrum with a LAPE response function of Eq. (8). We therefore fit this convolution to the combined ir-xuv photoemission spectrum, allowing the sideband intensities A_1 and A_2, as well as the width σ and the peak separation $\hbar\omega$, to be fit parameters. The factor in front of the first Gaussian peak is chosen to normalize the response function to 1. The parameters A_1 and A_2 thus give the fraction of electrons scattered into the first and second sidebands, respectively. Figure 8 shows the result for zero time delay between the ir and xuv beams. The dotted line gives the photoemission spectrum without the ir pulse present. The solid line shows the photoemission spectrum with the ir pulse present. Finally, the dashed line shows the
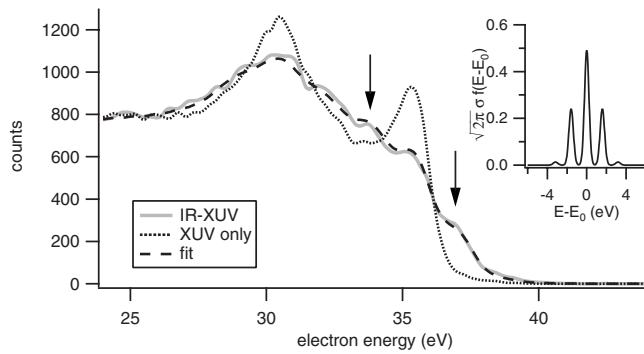
FIG. 8. Photoemission spectrum at zero time delay between the ir and xuv fields, taken from the data shown in Fig. 6. Observed photoemission spectrum with (solid line) and without (dotted line) the ir pulse present. The dashed line shows the fit to the ir-xuv curve by convolving the LAPE response function from Eq. (8) with the unperturbed spectrum. The inset shows the LAPE response function associated with the fit.

fit to the ir-xuv curve by convolving the LAPE response function from Eq. (8) with the unperturbed spectrum. The inset of Fig. 8 shows the LAPE response function associated with the resulting fit parameters: $A_1 = 0.241 \pm 0.004$, $A_2 = 0.013 \pm 0.003$, $\sigma = 0.23 \pm 0.02$ eV, and $\hbar\omega = 1.59 \pm 0.02$ eV. It is multiplied by $\sqrt{2\pi\sigma^2}$, so that the peak heights reflect the corresponding intensity parameters A_1 and A_2.

The fit to the sideband separation of $\hbar\omega = 1.59$ eV corresponds very well to the photon energy of the ir beam, while the width σ reflects closely the convolution of the laser bandwidth (≈ 0.1 eV) and the detector resolution at the high-energy part of the photoelectron spectrum (≈ 0.2 eV). Initially, we allowed the response function to be asymmetric using different intensity parameters $A_{1,2}^{\pm}$ for the positive and negative sidebands. However, this fit generally yielded sideband heights that were identical for the high- and low-energy sidebands, as would be expected for the LAPE in this weak-field regime (see Fig. 9). The quality of the resulting fit strongly supports the interpretation of these data as surface LAPE. This is further corroborated by the fact that no side-
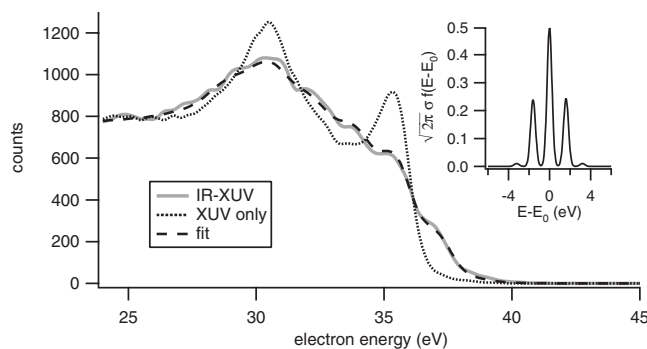

FIG. 9. Identical spectrum to that shown in Fig. 8, where the positive and negative first-order sideband heights are allowed to vary separately during the fit. However, no significant asymmetry is generated as a result of this fit.
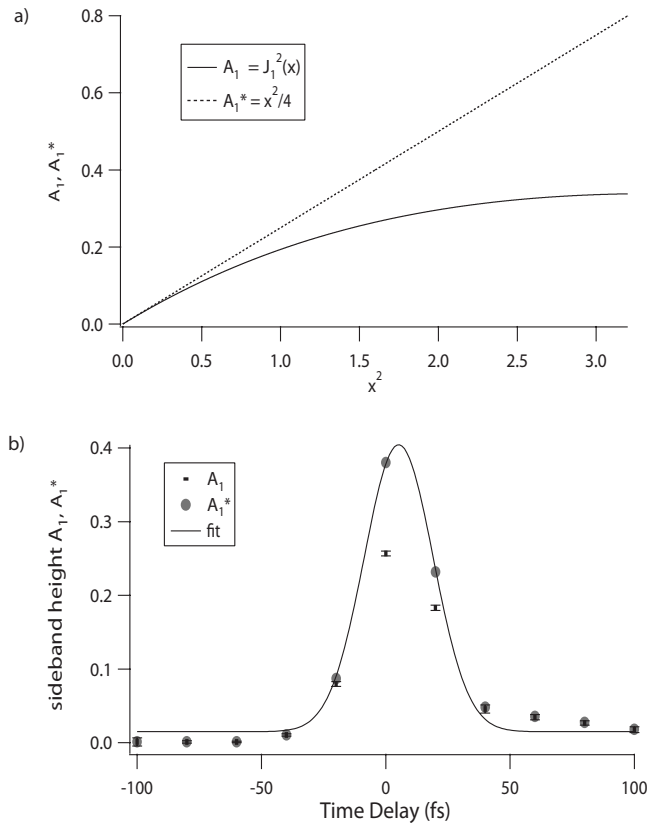

FIG. 10. (a) The solid line shows the square of the Bessel function $A_1 = J_1^2(x)$, plotted versus $x^2 \propto I$. The dotted line depicts the asymptote behavior for small x: $A_1^* = x^2/4$. For a cross-correlation measurement, a linear intensity dependence of A_1 is required, which is only fulfilled for small x. (b) Measured cross correlation of the ir (of duration around 35 fs) and the expected ≈ 10 fs duration xuv pulses as a function of time delay. The measured sideband heights A_1 are replaced by the corresponding values A_1^* of the asymptote, so that linear intensity dependence is ensured for all data points. A Gaussian fit yields 33 ± 2 fs, limited by the duration of the ir pulse duration. A Gaussian fit to the uncorrected A_1 data yields 37 ± 3 fs.

bands are observed when the polarization of the ir light is perpendicular to the direction of detection [s polarized, see Fig. 18(a)]. However, hot electrons can be observed for both polarizations of the ir field. These hot electron-energy distributions persist for significantly longer times than the LAPE response (hundreds of femtoseconds), and are discussed below.

By fitting the photoelectron spectra for all other time delays, with $\hbar\omega$ and σ fixed to the values derived from the time zero photoemission spectrum, we determine the strengths A_1 of the first-order sideband as a function of delay between the ir and xuv pulses [Fig. 10(b)]. The small error bars show the large sensitivity of the fit to the sideband heights, which is due to the fact that the positive sidebands show up in a region well beyond the Fermi edge, where the xuv-only spectrum only exhibits a small count rate. For a cross-correlation measurement, an observable which is linear in the laser intensity I_L is required. As shown in Fig. 10(a), A_1 fulfills this requirement for small I_L, where A_1 is approximated by the asymptote $A_1^* = x^2/4$, and, following Eq. (6), $x^2 \propto I_L$. For
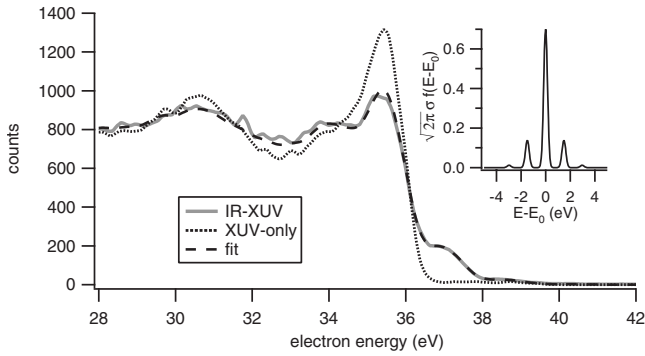
FIG. 11. LAPE spectrum taken at a different sample angle of 5°. Due to the larger *d*-band peak at this angle, the negative sideband is more clearly visible.

larger intensities, however, A_1 levels off and exhibits a sublinear behavior. To ensure a linear dependence for all data points, the sideband heights A_1 are thus replaced by the corresponding values A_1^* of the asymptote. A Gaussian fit yields a full width at half maximum of 33 ± 2 fs, in accordance with the expected xuv pulse duration of ~10 fs and the ir pulse duration of the order of 35 fs, respectively.

Figure 11 shows a LAPE measurement at an angle of about $\vartheta = 5°$ between the ir polarization (*p* polarized) and the surface normal, close to grazing incidence. At this sample angle, which corresponds to an observation angle of about 20° with respect to the surface normal, the *d*-band peak at the Fermi edge is even more pronounced than in the previous geometry, and it dominates the broader *d*-band structure at 30 eV. As a result, the sideband characteristics of the LAPE process become even more obvious. The steps due to the first- and second-order positive sidebands are more pronounced and the first-order negative sideband is visible. Moreover, like in the previous data set, the ir-xuv spectrum can again be reproduced from the xuv-only data by convolution with the symmetric sideband function of Eq. (8). This result has been found at several other sample angles as well, which are not shown here. The universal applicability of this fit procedure to data taken at different sample angles excludes band structure effects, e.g., the opening of band gaps [38,39], to be the cause for the observed ir-induced modifications to the photoemission spectra.

Figure 12 shows a time series of LAPE spectra (solid gray curves) between −40 fs and 40 fs in steps of 5 fs, taken at the new geometry ($\vartheta = 5°$). The dotted curves represent the xuv-only spectra and the dashed curves are the fits. In this data set, the space charge turns out to be stronger than in the previous measurement. This may be due to higher surface roughness, which depends on the cleaning procedure and thus changes from day to day. The corresponding shift to higher energies of the ir-xuv spectra with respect to the xuv-only curve is already corrected for in Fig. 12. In addition, the data at −40 fs (where the ir pulse comes after the xuv pulse) reveal a slight smearing of the ir-xuv spectrum, caused by the space-charge-induced Coulomb explosion. Despite this smearing, the fit procedure still qualitatively reproduces the ir-xuv spectra, especially the steplike structure in the spectra that show strong LAPE. Quantitatively however, the space-
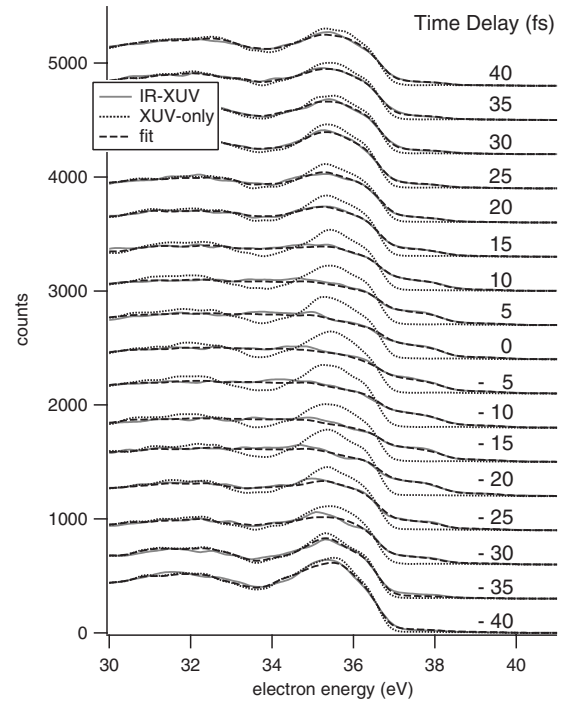

FIG. 12. LAPE time series for ir-xuv pulse separations between −40 fs and 40 fs in steps of 5 fs. The dotted lines show the xuv-only data. The ir-xuv spectra (solid gray lines) are corrected for a 0.1 eV space-charge shift. The dashed lines show the symmetric fits.

charge distortion will lead to systematic deviations of the fit parameters A_1 and A_2. These sideband heights are plotted versus time delay in Fig. 13. A_1 grossly follows the expected Gaussian cross-correlation characteristics as in the previous data set. However, it does not go to zero at the wings mainly because of the space-charge effects. Moreover, the background is not constant, but is higher for positive time delays. This background is most likely composed of a constant part due to the space-charge effect and, above time zero, a time-dependent part from hot electrons. We will discuss these effects in more detail in the following sections of this paper, but will not take it into account in the discussion of the
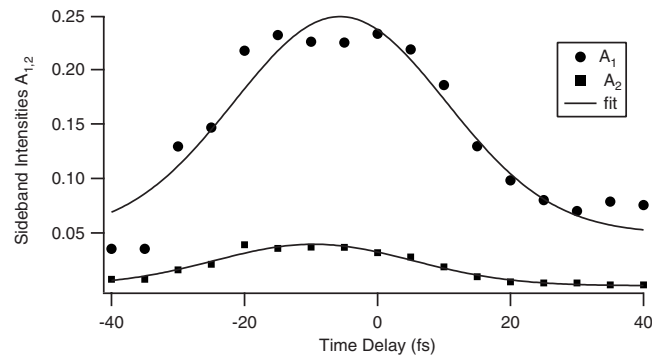

FIG. 13. Amplitude of the first-order (circles) and second-order (squares) sideband intensity versus time delay. The fits result in FWHM of 37 ± 5 fs and 35 ± 3 fs for the first- and second-order sidebands, respectively.
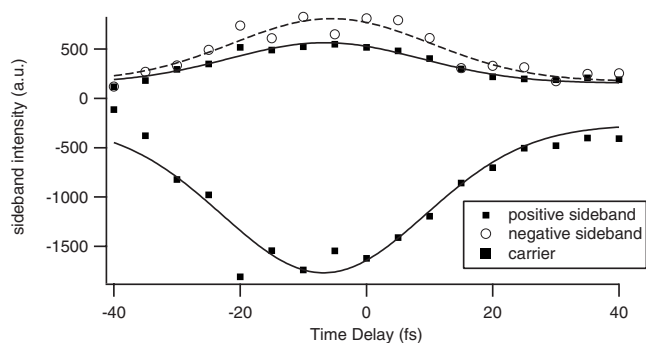
FIG. 14. Positive and negative sideband heights (upper curve) and depletion of the d-band peak (lower curve) versus time delay. The Gaussian fits (solid lines) yield 36 ± 4 fs for the positive sideband, 37 ± 6 fs for the negative sideband, and 38 ± 5 fs for the depletion signal, respectively.

present data set. A tentative Gaussian fit of the A_1 curve in Fig. 13 yields a width of 38 ± 5 fs, similar to the previous measurement.

Due to the larger number of data points, the present time series makes it possible to investigate the time dependence of the smaller second-order sideband height A_2 (see Fig. 13). It follows a similar Gaussian curve with a width of 35 ± 3 fs, in agreement with the time dependence expected from the pulse lengths. Moreover, despite the contributions from hot electrons and space charge, we can perform a coarse check of Eq. (5) by comparing the maxima of A_1 and A_2. For the observed $A_1^{\max} = 0.25 \pm 0.02$ we expect, after $A_n = J_n^2(x)$, an accompanying $A_2^{\max} = 0.026 \pm 0.06$, which agrees reasonably with the measured value of 0.038 ± 0.002.

Figure 14 shows an alternative analysis of the data using the d-band peak at the Fermi edge. After subtraction of the xuv-only curves in Fig. 12 from the xuv-ir data, two maxima arise around 34 and 37 eV, originating from the first- and second-order sideband, respectively. Additionally, the depletion of the d-band peak leads to a minimum in the subtracted data. These three extrema are plotted versus time delay in Fig. 14. Gaussian fits result in widths of 36 ± 4 fs for the positive sideband, 37 ± 6 fs for the negative sideband, and 38 ± 5 fs for the zeroth order, which agree with each other and with the pulse widths within their error margins. In summary, dressing of pronounced peaklike structures in the electron spectra of solids can be detected by a direct comparison of the xuv-only and the ir-xuv data and by monitoring the sideband heights or, more sensitively, by the depletion of the photoemission peak. Alternatively, if the structure is more complicated, the convolution of the xuv-only data with a sideband function has to fit to the ir-xuv data. In any case, the dressing makes it possible to, in principle, measure the time when electrons are ejected from surfaces or adsorbates by photoemission or subsequent Auger decay. To achieve optimum time resolution, other ir-induced effects such as space-charge acceleration or hot electron excitation must be minimized. One promising route to this goal is the use of longer wavelength ir light. Following Eq. (7), the required laser intensity to generate sidebands of a certain height is proportional to ω_{ir}^4. Figure 2 shows the intensity to generate
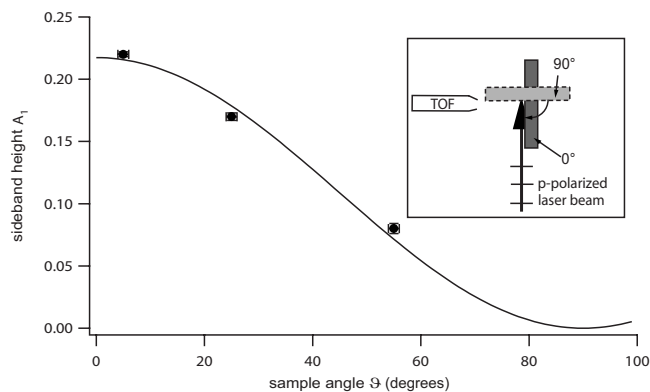

FIG. 15. First-order sideband height as a function of the sample angle. The sample is shown to influence the effective dressing field, because the component of the electric field perpendicular to the surface is reduced due to boundary conditions. The data agree with the expected $\cos^2$ reduction in the effective intensity. The inset illustrates the definition of the sample angle (surface normal) for $0°$ and $90°$ with respect to the ir polarization.

$A_1 = 0.1$ for a wavelength of 1600 nm, which could be reached by a high-intensity optical-parametric amplifier [46]. Compared to 800 nm, as used in this work, 16 times less intensity is needed. This would diminish most other effects dramatically.

As scattering of photoemitted electrons within the material leads to large angle and energy changes, scattered electrons are effectively removed from the part of the spectrum near the Fermi edge that we analyze. The observed electrons thus essentially originate from a thin layer defined by their ≈ 5 Å mean free path. We believe that the finite transit time through this layer ultimately limits the resolution of surface LAPE for characterizing xuv pulses or for measuring ultrafast inner-shell electron dynamics in solids. In our case, this value is < 200 attoseconds, and thus does not limit our measurement. Still higher resolution could be obtained by increasing the xuv photon energy, and thus the emitted photoelectron energies, so that they escape more quickly. Therefore, this result also opens up new possibilities for studying femtosecond-to-attosecond correlated electron dynamics in solids.

C. Laser intensity dependence of LAPE from surfaces

To study the intensity dependence of the first-order sidebands, we first investigated the influence of the sample on the effective intensity on the surface. To this end, the ir light was p polarized and the surface was rotated horizontally to three different angles ϑ between the ir polarization and the surface normal. $\vartheta = 0°$ denotes grazing incidence with the polarization being perpendicular to the surface. $\vartheta = 90°$ denotes normal incidence and parallel polarization with respect to the surface. Figure 15 shows the amplitude A_1 of the first-order sideband extracted at three different angles. Towards $\vartheta = 90°$, A_1 decreases strongly. This sample angle dependence can be fit with a $\cos^2$ consistent with the assumption that only the electric field exactly at the surface interacts with
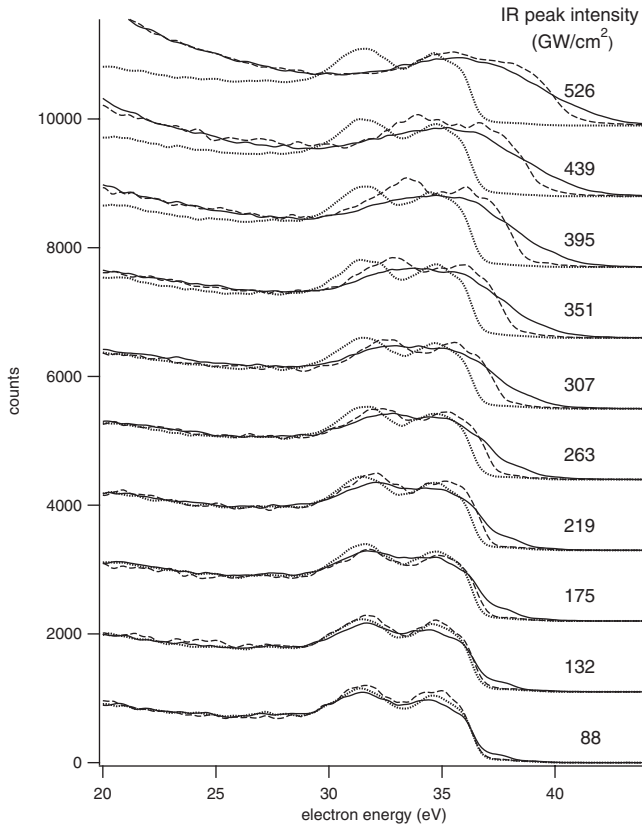
FIG. 16. Photoemission due to both ir-xuv (solid lines) and xuv-only (dotted lines) light at time zero as well as ir-xuv for a delay of −100 fs (dashed) for different ir laser intensities. The −100 fs curves show the influence of the space charge induced by the ir-induced low-energy electrons on the xuv photoelectrons around the Fermi edge. At low intensities, it results in a shift to higher energies due to acceleration. At the highest intensity shown, the space charge also changes the shape of the spectrum.

the photoemitted electron. As the parallel component $E_{\parallel}$ vanishes here, only the perpendicular field $E_{\perp} = E_{in} \cos \vartheta$ remains. For moderate laser intensities, A_1 is linear in I_L and therefore follows $I_{in} \cos^2 \vartheta$.

Figure 16 depicts a series of photoemission spectra taken at different ir peak intensities. ir-xuv (solid lines) and xuv-only (dotted lines) at time zero as well as ir-xuv at −100 fs time delay (dashed) are shown. The −100 fs curves reflect the influence of the space charge of the ir-induced low-energy electrons on the xuv photoelectrons around the Fermi edge. At low intensities, it results in a shift to higher energies due to acceleration, whereas the shape of the spectrum is unaffected. At the highest intensity shown, the space charge also changes the shape of the spectrum. After correcting for the space-charge shifts using the −100 fs spectra, the sideband heights A_1 are determined using the fit procedure described above. The results are shown in Fig. 17. The measurement taken near 600 GW/cm² is still below the damage threshold of the surface. However, at this intensity the space charge created by the ir beam on the sample starts changing the shape of the ir-xuv spectrum as compared to the xuv-only one, making the extraction of the sideband amplitude more difficult. We thus used a ir-xuv spectrum taken at −100 fs as
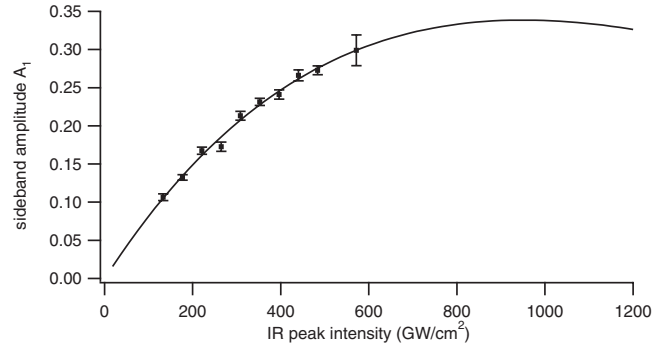

FIG. 17. Extracted sideband intensity A_1 as a function of the effective ir beam peak intensity, perpendicular to the surface. The influence of the sample angle has been taken into account. The sideway intensity follows the theoretically expected square of the first-order Bessel function. The position of the maximum of the curve is by about a factor of 2 higher than expected from the argument of the Bessel function [Eq. (6)]. This is within our experimental uncertainty in the determination of the effective dressing intensity, because of insufficient knowledge of the spatial overlap between ir and xuv pulses on the sample.

a background spectrum for the convolution, since it shows the same distortions due to the space-charge effect as the ir-xuv spectrum but does not exhibit the sidebands. This procedure leads to the larger uncertainty for this data point. At even higher laser intensities, electrons from ATP begin to overlap with the Fermi edge in the spectra, and bury the LAPE signature. However, such high laser intensities are only necessary for testing the validity of the simple theoretical description of surface LAPE given earlier.

The laser intensity is also corrected for the sample angle, so that it corresponds to the perpendicular component of the electric field. This corrected laser-intensity dependence is then fit to $A_n = J_n^2(a\sqrt{I})$. Here, a is a fit parameter and $n=1$ denotes the number of absorbed or emitted ir photons. Qualitatively, we find excellent agreement between our data and this model. The quantitative comparison is limited by the knowledge of the actual ir beam intensity. We calculated the peak ir intensity corresponding to the perpendicular electric field at the surface by taking into account the sample angle. This intensity is likely to be an overestimation of the effective dressing intensity for two reasons. First, the xuv beam spot size is estimated to be a significant fraction of the ir beam spot size. And second, a possible misalignment of the spatial ir-xuv overlap would decrease the effective intensity. From the kinetic energies of the electrons around the Fermi edge and the laser photon energy, the first-order sideband amplitude is expected to peak at 540 GW/cm². From the fit we find the maximum of the Bessel function at 960 GW/cm², which is within our error margin for the effective intensity. Note also that our highest data point has an amplitude of $A_1 = 0.30$, very close to the maximum of the square of the first-order Bessel function of 0.348. This shows that essentially all detected photoelectrons are dressed.

For applications such as measurement of pulse duration or surface electron dynamics, it is desirable to use lower IR pulse intensities in the linear regime, where the cross-
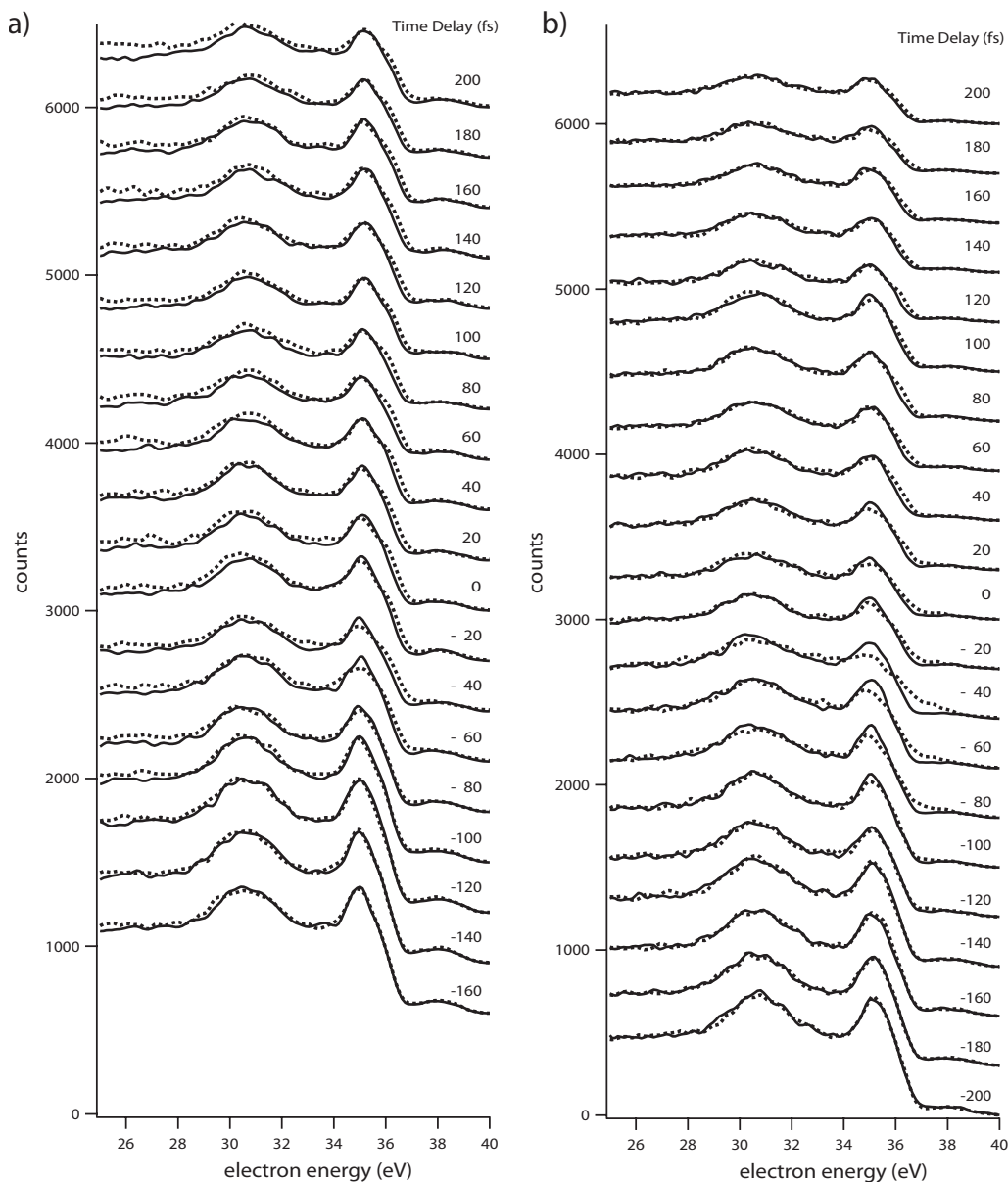
FIG. 18. (a) Photoemission spectra around the Fermi edge for *s*-polarized ir light at high laser intensity (10^{12} W/cm^2). The electric field at the surface vanishes in this case, so that no dressing is expected. However, due to the absorption of ir light, a hot electron distribution is excited, and is visible at the Fermi edge for relative time delays later than −60 fs (time zero in this measurement). (b) Photoemission spectra for *p*-polarized ir light at half the intensity applied in (a) (5×10^{11} W/cm^2). Hot electrons are visible at positive time delays. LAPE can be observed at −40 fs (time zero), clearly dominating the hot electron distribution and distinguishable by its steplike shape.

correlation $A_1(\tau)$ directly reflects the time behavior under study. At these laser intensities, we found LAPE to be the dominant process. The presence of space charge induces only a small overall shift in the spectra that can be corrected for. Above-threshold photoemission can be suppressed below 600 GW/cm^2 by using a flat surface [42]. The excitation of hot electrons has been found to cause significantly smaller modifications of the photoemission spectrum than LAPE even at rather high laser intensities. However, the presence of such hot electrons can be distinguished from LAPE since their presence increases the average electron kinetic energy around the Fermi edge.

In conclusion, our data show that laser-assisted photoemission from a Pt(111) surface can be observed for ir intensities up to 600 GW/cm^2, below what is needed to observe heating, ATP, or desorption at metal surfaces [8]. This result is important for applications of surface LAPE to the study of attosecond electron dynamics in solids and in surface-adsorbate systems.

D. Hot electrons

At high ir laser intensities ($I_L > 5 \times 10^{11}$ W/cm^2), a significant number of electrons within the conduction band will
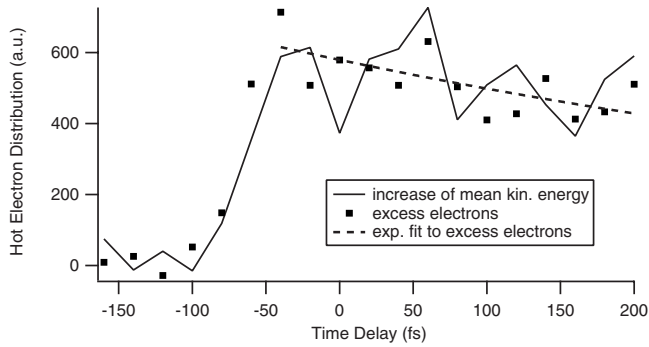
FIG. 19. Excess hot electrons (dots) at the Fermi edge for *s*-polarized ir light. These hot electrons follow a sharp rise and slow exponential decay. The fit (dashed line) yields a lifetime of about 270 ± 60 fs. This behavior is also found for the average kinetic energy (solid line) and is consistent with expected hot electron lifetimes.

be excited, resulting in a nonequilibrium hot electron distribution at the Fermi edge. The number of excited electrons depends only on the laser fluence absorbed by the metal. Hot electron excitation is thus expected regardless of the polarization, although energy coupling into the surface can vary (to some extent) with polarization. In order to observe hot electrons—but suppress LAPE—we acquired the time series of photoemission spectra shown in Fig. 18(a) using *s*-polarized ir light at a high intensity of about 10^{12} W/cm^2. For time delays greater than -60 fs, a slight influence of the ir laser light is observed in the ir-xuv spectra. However, this effect is considerably smaller than in the previous measurements with *p*-polarized light. We analyze these excess electrons in two different ways. First we subtracted the xuv-only spectra from the corresponding ir-xuv spectra. These difference spectra show a peak above the Fermi edge stemming from the excess electrons. Figure 19 shows the integrated area of this peak versus time delay. The second approach to analyze these data is by calculating the average kinetic energies $\langle E_{kin,ir} \rangle$ and $\langle E_{kin,xuv} \rangle$ above the ATP distribution (i.e., >33 eV in this case). In Fig. 19, the solid line shows, as a function of time delay, the normalized difference $(\langle E_{kin,ir} \rangle - \langle E_{kin,xuv} \rangle)/\langle E_{kin,xuv} \rangle$, i.e., the laser-induced increase of the kinetic energy. After proper scaling, the curves are shown to follow the same characteristics: an increase in electrons $>E_F$ at -60 fs followed by an exponential decay as the time delay increases. Since for positive time delays, the ir pulse comes first, it obviously serves as a pump for the process observed here. This time behavior is fundamentally different from the cross correlation found for LAPE, and indicates the excitation of a comparatively long-lived hot electron distribution.

Figure 18(b) shows another time series taken with *p*-polarized ir light at a laser intensity of 5×10^{11} W/cm^2, which is half the intensity used with the *s*-polarized light data discussed above. These data clearly show a LAPE signal at -40 fs, visible again as a comparably strong steplike modification of the Fermi edge. In additions excess electrons are visible beyond the Fermi edge for time delays exceeding the ir-xuv cross-correlation time. We again corrected for the small space-charge effect and then evaluated the excess elec-
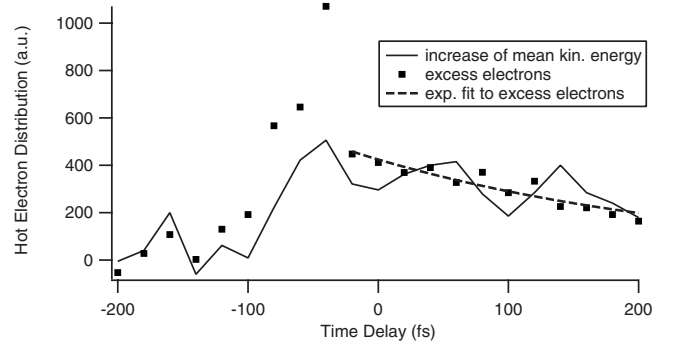

FIG. 20. Excess hot electrons (dots) at the Fermi edge for *p*-polarized ir light. In this case, the excess electrons show a two-component structure. For large time delays they decay exponentially. The fit results in a lifetime of 260 ± 80 fs, in agreement with the value found for *s*-polarized light (270 ± 60 fs). Around time zero, the electron distribution exhibits a peak which is due to LAPE. The average kinetic energy, which is insensitive to LAPE, still follows the exponential decay behavior characteristic of hot electron decay.

trons and the kinetic energy increase (Fig. 20). In this measurement, the time dependence of the excess electrons exhibits a two-component structure. We ascribe the peak at -40 fs to LAPE. The corresponding spectrum could be fitted in the way described above. The subsequent slow decay is due to hot electrons. A fit yields a decay time of about 260 fs, in agreement with the measurement using *s*-polarized light. The kinetic energy curve reflects only the hot electron contribution to the excess electrons since LAPE does not change the net kinetic energy. This shows that the slow decay can be attributed to electrons that on average gain kinetic energy, whereas the peak is due to electrons that are redistributed symmetrically due to LAPE.

V. CONCLUSIONS AND OUTLOOK

In conclusion, we have investigated the laser-assisted photoelectric effect from a solid surface. By illuminating a Pt(111) sample simultaneously with ultrashort 1.6 and 42 eV pulses, we observed sidebands in the extreme ultraviolet photoemission spectrum. Sideband amplitudes were extracted very accurately from the continuous spectra over a wide range of laser intensities. Our results agree with a simple model, in which LAPE is described by xuv photoemission followed by the interaction of the photoemitted electron with the laser field. This strong effect can definitively be distinguished from other laser surface interaction phenomena, such as hot electron excitation, above-threshold photoemission, and space-charge acceleration. As a consequence, laser-assisted photoemission from surfaces promises to be useful to extend xuv pulse duration measurements to higher photon energies, as well as opening up femtosecond-to-attosecond time-scale electron dynamics in solid and surface-adsorbate systems.

[1] Z. Chang, A. Rundquist, H. Wang, M. Murnane, and H. Kapteyn, Phys. Rev. Lett. **79**, 2967 (1997).

[2] C. Spielmann, N. H. Burnett, S. Sartania, R. Koppitsch, M. Schnürer, C. Kan, M. Lenzner, P. Wobrauschek, and F. Krausz, Science **278**, 661 (1997).

[3] H. C. Kapteyn, M. M. Murnane, and I. P. Christov, Phys. Today **58** (3), 39 (2005).

[4] F. Quere, S. Guizard, P. Martin, G. Petite, H. Merdji, B. Carré, J.-F. Hergott, and L. Le Déroff, Phys. Rev. B **61**, 9883 (2000).

[5] A. Rettenberger, P. Leiderer, M. Probst, and R. Haight, Phys. Rev. B **56**, 12092 (1997).

[6] S. Passlack, S. Mathias, O. Andreyev, D. Mittnacht, M. Aeschlimann, and M. Bauer, J. Appl. Phys. **100**, 024912 (2006).

[7] K. Read, H. S. Karlsson, M. M. Murnane, H. C. Kapteyn, and R. Haight, J. Appl. Phys. **89**, 294 (2001).

[8] M. Bauer, C. Lei, K. Read, R. Tobey, J. Gland, M. M. Murnane, and H. C. Kapteyn, Phys. Rev. Lett. **87**, 025501 (2001).

[9] R. I. Tobey, E. H. Gershgoren, and M. E. Siemens *et al.*, in *Ultrafast Phenomena XIV*, edited by T. Kobayashi, T. Okada, T. Kobayashi, K. A. Nelson, and S. D. Silvestri (Springer-Verlag, Niigata, Japan, 2004), p. WC3.

[10] L. Nugent-Glandorf, M. Scheer, D. Samuels, V. M. Bierbaum, and S. R. Leone, J. Chem. Phys. **117**, 6108 (2002).

[11] E. Gagnon, P. Ranitovic, A. Paul, C. Lewis Cocke, M. M. Murnane, H. C. Kapteyn, and A. S. Sandhu, Science **317**, 1374 (2007).

[12] A. Weingartshofer, J. K. Holmes, G. Caudle, E. M. Clarke, and H. Krüger, Phys. Rev. Lett. **39**, 269 (1977).

[13] J. M. Schins, P. Breger, P. Agostini, R. C. Constantinescu, H. G. Muller, G. Grillon, A. Antonetti, and A. Mysyrowicz, Phys. Rev. Lett. **73**, 2180 (1994); Phys. Rev. A **52**, 1272 (1995).

[14] M. M. Murnane, H. C. Kapteyn, and R. W. Falcone, Phys. Rev. Lett. **62**, 155 (1989).

[15] T. E. Glover, R. W. Schoenlein, A. H. Chin, and C. V. Shank, Phys. Rev. Lett. **76**, 2468 (1996).

[16] M. Drescher, M. Hentschel, R. Kienberger, M. Uiberacker, V. Yakovlev, A. Scrinzi, Th. Westerwalbesloh, U. Kleineberg, U. Heinzmann, and F. Krausze, Nature (London) **419**, 803 (2002).

[17] P. M. Paul, E. S. Toma, P. Breger, G. Mullot, F. Augé, Ph. Balcou, H. G. Muller, and P. Agostini, Science **292**, 1689 (2001).

[18] A. Baltuška, Th. Udem, M. Uiberacker, M. Hentschel, E. Goulielmakis, Ch. Gohle, R. Holzwarth, V. S. Yakovlev, A. Scrinzi, T. W. Hänsch, and F. Krausz, Nature (London) **421**, 611 (2003).

[19] M. Hentschel, R. Kienberger, Ch. Spielmann, G. A. Reider, N. Milosevic, T. Brabec, P. Corkum, U. Heinzmann, M. Drescher, and F. Krausz, Nature (London) **414**, 509 (2001).

[20] R. Kienberger, E. Goulielmakis, M. Uiberacker, A. Baltuska, V. Yakovlev, F. Bammer, A. Scrinzi, Th. Westerwalbesloh, U. Kleineberg, U. Heinzmann, M. Drescher, and F. Krausz, Nature (London) **427**, 817 (2004).

[21] J. Itatani, F. Quéré, G. L. Yudin, M. Yu. Ivanov, F. Krausz, and P. B. Corkum, Phys. Rev. Lett. **88**, 173903 (2002).

[22] M. Meyer, D. Cubaynes, P. O'Keeffe, H. Luna, P. Yeates, E. T. Kennedy, J. T. Costello, P. Orr, R. Taïeb, A. Maquet, S. Düsterer, P. Radcliffe, H. Redlin, A. Azima, E. Plönjes, and J. Feldhaus, Phys. Rev. A **74**, 011401(R) (2006).

[23] L. Miaja-Avila, C. Lei, M. Aeschlimann, J. L. Gland, M. M. Murnane, H. C. Kapteyn, and G. Saathoff, Phys. Rev. Lett. **97**, 113604 (2006).

[24] A. L. Cavalieri, N. Müller, Th. Uphues, V. S. Yakovlev, A. Baltuska, B. Horvath, B. Schmidt, L. Blümel, R. Holzwarth, S. Hendel, M. Drescher, U. Kleineberg, P. M. Echenique, R. Kienberger, F. Krausy, and U. Heinzmann, Nature (London) **449**, 1029 (2007).

[25] T. Sekikawa, A. Kosuge, T. Kanai, and S. Watanabe, Nature (London) **432**, 605 (2004).

[26] P. Tzallas, D. Charalambidis, N. A. Papadogiannis, K. Witte, and G. D. Tsakiris, Nature (London) **426**, 267 (2003).

[27] H. R. Reiss, Phys. Rev. A **22**, 1786 (1980).

[28] H. G. Muller, H. B. van Linden van den Heuvell, and M. J. Van der Wiel, J. Phys. B **19**, L733 (1986).

[29] L. B. Madsen, Am. J. Phys. **73**, 57 (2005).

[30] M. P. Seah and W. A. Dench, Surf. Interface Anal. **1**, 2 (1979).

[31] S. Tanuma, T. Shiratori, T. Kimura, K. Goto, S. Ichimura, and C. J. Powell, Surf. Interface Anal. **37**, 833 (2005).

[32] B. Feuerbacher and R. F. Willis, J. Phys. C **9**, 169 (1976).

[33] R. Haydock and M. J. Kelly, Surf. Sci. **38**, 139 (1973).

[34] A. Cionga, V. Florescu, A. Maquet, and R. Taieb, Phys. Rev. A **47**, 1830 (1993).

[35] A. Mönnich, J. Lange, M. Bauer, M. Aeschlimann, I. A. Nechaev, V. P. Zhukov, P. M. Echenique, and E. V. Chulkov, Phys. Rev. B **74**, 035102 (2006).

[36] J. E. Bayfield, L. D. Gardner, Y. Z. Gulkok, and S. D. Sharma, Phys. Rev. A **24**, 138 (1981).

[37] H. R. Reiss, Phys. Rev. A **39**, 2449 (1989).

[38] N. Tzoar and J. I. Gersten, Phys. Rev. B **12**, 1132 (1975).

[39] F. H. M. Faisal and J. Z. Kamiński, Phys. Rev. A **56**, 748 (1997).

[40] S. H. Autler and C. H. Townes, Phys. Rev. **100**, 703 (1955).

[41] G. Leschik, R. Courths, H. Wern, S. Hüfner, H. Eckardt, and J. Noffke, Solid State Commun. **52**, 221 (1984).

[42] M. Aeschlimann, C. A. Schmuttenmaer, H. E. Elsayed-Ali, R. J. D. Miller, J. Cao, Y. Gao, and D. A. Mantell, J. Chem. Phys. **102**, 8606 (1995).

[43] G. Petite, P. Agostini, R. Trainham, E. Mevel, and P. Martin, Phys. Rev. B **45**, 12210 (1992).

[44] S. Backus, R. Bartels, S. Thompson, R. Dollinger, H. C. Kapteyn, and M. M. Murnane, Opt. Lett. **26**, 465 (2001).

[45] A. Rundquist, C. G. Durfee III, Z. Chang, C. Herne, S. Backus, M. M. Murnane, and H. C. Kapteyn, Science **280**, 1412 (1998).

[46] B. Shan, A. Cavalieri, and Z. Chang, Appl. Phys. B: Lasers Opt. **74**, S23 (2002).

[47] P. Siffalovic, M. Drescher, M. Spieweck, T. Wiesenthal, Y. C. Lim, R. Weidner, A. Elizarov, and U. Heinzmann, Rev. Sci. Instrum. **72**, 30 (2001).